

A corrected transport-velocity formulation for fluid and structural mechanics with SPH

Dinesh Adep^{a,*}, Prabhu Ramachandran^a

^a*Department of Aerospace Engineering, Indian Institute of Technology Bombay, Powai, Mumbai 400076*

Abstract

Particle shifting techniques (PST) have been used to improve the accuracy of the Smoothed Particle Hydrodynamics (SPH) method. Shifting ensures that the particles are distributed homogeneously in space. This may be performed by moving the particles using a transport velocity. In this paper we propose an extension to the class of Transport Velocity Formulation (TVF) methods. We derive the equations in a consistent manner and show that there are additional terms that significantly improve the accuracy of the method. In particular, we apply this to the Entropically Damped Artificial Compressibility SPH method. We identify the free-surface particles and their normals using a simple approach and thereby adapt the method for free-surface problems. We show how the new method can be applied to the problem of elastic dynamics. We consider a suite of benchmark problems involving both fluid and solid mechanics to demonstrate the accuracy and applicability of the method. The implementation is open source and the manuscript is fully reproducible.

Keywords: SPH, free surface, solid mechanics, fluid mechanics, weakly-compressible, transport velocity

1. Introduction

The smoothed particle hydrodynamics (SPH) method has been widely applied since it was originally proposed to simulate hydrodynamic problems in

*Corresponding author

Email addresses: adepu.dinesh.a@gmail.com (Dinesh Adep),
prabhu@aero.iitb.ac.in (Prabhu Ramachandran)

astrophysics independently by Lucy [1], and Gingold and Monaghan [2]. The method has been applied in particular to both compressible [3], incompressible fluid flows [4, 5] as well as elastic dynamics problems [6, 7] in addition to a variety of other problems[8, 9, 10, 11].

The method is meshless and Lagrangian, and therefore particles move with the local velocity. This motion can introduce disorder in the particles and thereby significantly reduce the accuracy of the method. Xu et al. [12] proposed an approach to shift the particles so as to obtain a uniform distribution of particles. This significantly improves accuracy and the method is referred to as the Particle Shifting Technique (PST). Many different kinds of PST methods are available in the literature [13, 14, 15, 16]. An alternative approach that ensures particle homogenization for incompressible fluid flow was proposed as the Transport Velocity Formulation (TVF) [17]. The method introduced an additional stress term to reduce errors introduced by the particle shifting. The TVF produces very accurate results but only works for internal flows. Zhang et al. [18] proposed the Generalized Transport Velocity Formulation (GTVF) thereby allowing the TVF to be used for free-surface problems as well as elastic dynamics problems. This allows for a unified treatment of both fluids and solids. Similarly, Oger et al. [19] introduce ideas from a consistent ALE formulation for improving the accuracy of SPH. They employ a Riemann-based formulation to solve fluid mechanics problems and introduce particle shifting to obtain highly accurate simulations for internal and free-surface problems may also be handled. The PST has also been employed in the context of the δ -SPH schemes[20].

The Entropically Damped Artificial Compressibility SPH scheme (EDAC-SPH) [21] introduces an evolution equation for the pressure and significantly reduces the noise in the pressure since it features a pressure diffusion term. The approach has a thermodynamic justification [22] and produces very accurate results [21]. The EDAC-SPH method uses the TVF formulation for internal flows and for free-surface flows it does not employ any form of particle shifting.

Recently, Antuono et al. [23] carefully combine the ALE-SPH method of Oger et al. [19] and the consistent δ -SPH formulation of Sun et al. [20] to improve the accuracy of the δ -SPH method. They show the importance of the additional terms to the accuracy.

With the notable exception of the GTVF scheme [18], most other applications of the PST have been in the context of fluid mechanics. The GTVF method provides a unified approach to solve both weakly-compressible flu-

ids as well as solids. However, the method suffers from a few issues. In order to work for free-surface problems the method relies on using a different background pressure for each particle and introduces a few numerical corrections to work around issues. For example, the smoothing length of the homogenization force is different from that used by the other equations and this parameter is somewhat ad-hoc. For solid mechanics problems the method uses the transport velocity of the particle rather than the true velocity in order to compute the strain and rotation tensor. In addition there are some terms in the governing equations that are ignored which play a major role. We also note that the method is not robust to a change in the particle homogenization force.

In this work we propose a scheme which we called Corrected Transport Velocity Formulation (CTVF) that is inspired by the various recent developments but is consistent and which works for both solid mechanics and fluid mechanics problems. We derive the transport velocity equations afresh and note that there are some important terms that are ignored in earlier approaches using TVF. These terms are significant and improve the accuracy of the method. Similar to [19, 20], we detect the free surface particles and compute their normals using a simpler and computationally efficient approach which does not require the computation of eigenvalues. This allows the method to work with free-surfaces without the introduction of numerical parameters or a variable background pressure. We employ the EDAC formulation and show that there are additional correction terms in the EDAC scheme that should be introduced to improve the accuracy of the method. Furthermore, we show how the EDAC scheme can be used in the context of solid mechanics problems. We make use of the particle velocity rather than the transport velocity to compute the velocity gradient, strain, and rotation rate tensors. Our method can be used with any PST and we consider the traditional TVF homogenization force, the method of Sun et al. [20] as well as the method of Huang et al. [15]. The method is also robust to the choice of the smoothing kernel. The resulting method works for both weakly-compressible fluids as well as solids. The new method may be thought of as an improved extension of the EDAC-SPH method that can be used for free-surface problems as well as solid mechanics problems.

The method is implemented using the PySPH framework [24, 25]. The source code for all the problems demonstrated in this manuscript is made available at <https://gitlab.com/pypr/ctvf>. Every result produced in the manuscript is fully automated using the `automan` package [26].

We next discuss the formulation for fluid mechanics as well as solid mechanics along with the use of particle shifting. The consistent correction terms are derived. We then consider a suite of benchmark problems for both fluids and solids and compare our results with those of other methods where applicable.

2. Governing equations

For elastic dynamics we use the same equations as in [7, 18] which we summarize below. The governing equations of motion involve the conservation of mass, which is in Lagrangian form is,

$$\frac{d\rho}{dt} = -\rho \frac{\partial u_i}{\partial x_i}, \quad (1)$$

and conservation of linear momentum,

$$\frac{du_i}{dt} = \frac{1}{\rho} \frac{\partial \sigma_{ij}}{\partial x_j} + g_i, \quad (2)$$

where ρ is the density, u_i is the i^{th} component of the velocity field, x_j is the j^{th} component of the position vector, g_i is the component of body force per unit mass and σ_{ij} is stress tensor.

The stress tensor is split into isotropic and deviatoric parts,

$$\sigma_{ij} = -p \delta_{ij} + \sigma'_{ij}, \quad (3)$$

where p is the pressure, δ_{ij} is the Kronecker delta function, and σ'_{ij} is the deviatoric stress.

The Jaumann's formulation for Hooke's stress provides us with the rate of change of deviatoric stress,

$$\frac{d\sigma'_{ij}}{dt} = 2G(\dot{\epsilon}_{ij} - \frac{1}{3}\dot{\epsilon}_{kk}\delta_{ij}) + \sigma'_{ik}\Omega_{jk} + \Omega_{ik}\sigma'_{kj}, \quad (4)$$

where G is the shear modulus, $\dot{\epsilon}_{ij}$ is the strain rate tensor,

$$\dot{\epsilon}_{ij} = \frac{1}{2} \left(\frac{\partial u_i}{\partial x_j} + \frac{\partial u_j}{\partial x_i} \right), \quad (5)$$

and Ω_{ij} is the rotation tensor,

$$\Omega_{ij} = \frac{1}{2} \left(\frac{\partial u_i}{\partial x_j} - \frac{\partial u_j}{\partial x_i} \right). \quad (6)$$

For a weakly-compressible or incompressible fluid the deviatoric stress vanishes and a viscous force is added to the stress tensor:

$$\sigma_{ij} = -p\delta_{ij} + 2\eta \frac{\partial u_i}{\partial x_j} \quad (7)$$

where η is the kinematic viscosity of the fluid.

In both fluid and solid modelling the pressure is computed using an isothermal equation of state, given as,

$$p = K \left(\frac{\rho}{\rho_0} - 1 \right), \quad (8)$$

where $K = \rho_0 c_0^2$ is the bulk modulus. Here, the constants c_0 and ρ_0 are the reference speed of sound and density, respectively. For solids, c_0 is computed as $\sqrt{\frac{E}{3(1-2\nu)\rho_0}}$, ν is the Poisson ratio.

3. Numerical method

Following the TVF [17] and similar formulations [19], we move the particles with a *transport velocity*, $\tilde{\mathbf{u}}$. The material derivative in this case is written as,

$$\frac{\tilde{d}}{dt} = \frac{\partial}{\partial t} + \tilde{u}_j \frac{\partial}{\partial x_j}. \quad (9)$$

We therefore recast the governing equations to incorporate the transport velocity starting with the conservation of mass, equation (1),

$$\frac{\tilde{d}\rho}{dt} = -\rho \frac{\partial u_j}{\partial x_j} + (\tilde{u}_j - u_j) \frac{\partial \rho}{\partial x_j}. \quad (10)$$

Since,

$$(\tilde{u}_j - u_j) \frac{\partial \rho}{\partial x_j} = \frac{\partial(\rho(\tilde{u}_j - u_j))}{\partial x_j} - \rho \frac{\partial(\tilde{u}_j - u_j)}{\partial x_j}, \quad (11)$$

we write equation (10), as

$$\frac{\tilde{d}\rho}{dt} = -\rho \frac{\partial \tilde{u}_j}{\partial x_j} + \frac{\partial(\rho(\tilde{u}_j - u_j))}{\partial x_j}. \quad (12)$$

By combining the continuity equation (1) and momentum equation (2) one can obtain the conservative form of the momentum equation as,

$$\begin{aligned} \frac{\partial(\rho u_i)}{\partial t} + \frac{\partial}{\partial x_j}(\rho u_i u_j) &= \rho g_i + \frac{\partial \sigma_{ij}}{\partial x_j} \\ &= \text{RHS}_i, \end{aligned} \quad (13)$$

where g_i is the body force acceleration, and σ_{ij} the stress tensor. We write the left hand side in terms of a transport derivative as,

$$\frac{\tilde{d}(\rho u_i)}{dt} + (u_j - \tilde{u}_j) \frac{\partial}{\partial x_j}(\rho u_i) + \rho u_i \frac{\partial u_j}{\partial x_j} = \text{RHS}_i. \quad (14)$$

Similar to eq. (11), we write,

$$(\tilde{u}_j - u_j) \frac{\partial}{\partial x_j}(\rho u_i) = \frac{\partial}{\partial x_j}(\rho u_i(\tilde{u}_j - u_j)) - \rho u_i \frac{\partial}{\partial x_j}(\tilde{u}_j - u_j). \quad (15)$$

Substituting, this in eq. (14), we have,

$$\frac{\tilde{d}(\rho u_i)}{dt} = \frac{\partial}{\partial x_j}(\rho u_i(\tilde{u}_j - u_j)) - \rho u_i \frac{\partial}{\partial x_j}(\tilde{u}_j) + \text{RHS}_i. \quad (16)$$

In Adami et al. [17], the second term is neglected but at this stage we do not neglect this term. We simplify this further and write,

$$\rho \frac{\tilde{d}u_i}{dt} + u_i \frac{\tilde{d}\rho}{dt} = \frac{\partial}{\partial x_j}(\rho u_i(\tilde{u}_j - u_j)) - \rho u_i \frac{\partial}{\partial x_j}(\tilde{u}_j) + \text{RHS}_i. \quad (17)$$

Using, eq. (12), we write

$$\begin{aligned} \rho \frac{\tilde{d}u_i}{dt} &= \frac{\partial}{\partial x_j}(\rho u_i(\tilde{u}_j - u_j)) - u_i \frac{\partial}{\partial x_j}(\rho(\tilde{u}_j - u_j)) + \text{RHS}_i \\ &= \rho(\tilde{u}_j - u_j) \frac{\partial u_i}{\partial x_j} + \text{RHS}_i \\ &= \rho \frac{\partial}{\partial x_j}(u_i(\tilde{u}_j - u_j)) - \rho u_i \frac{\partial}{\partial x_j}(\tilde{u}_j - u_j) + \text{RHS}_i. \end{aligned} \quad (18)$$

We therefore write the momentum equation as,

$$\frac{d\tilde{u}_i}{dt} = \frac{\partial}{\partial x_j} (u_i(\tilde{u}_j - u_j)) - u_i \frac{\partial}{\partial x_j} (\tilde{u}_j - u_j) + g_i + \frac{1}{\rho} \frac{\partial \sigma_{ij}}{\partial x_j}. \quad (19)$$

We note that this equation encompasses both fluid dynamics as well as elastic dynamics by simply changing the way σ_{ij} is modeled. The first term on the right-hand-side of eq. (19) is the additional artificial stress term that is included in the TVF [17]. The second term involves the divergence of the transport velocity field. In the case of the TVF, the term includes a background pressure acceleration that is of the form,

$$\left(\frac{d\mathbf{u}_a}{dt} \right)_c = -p_a^0 \sum_{b \in N(a)} \frac{m_b}{\rho_b^2} \nabla W(\mathbf{r}_{ab}, \tilde{h}_{ab}), \quad (20)$$

where p_a^0 is the background pressure for the given particle a , $\mathbf{r}_{ab} = \mathbf{r}_a - \mathbf{r}_b$, $\tilde{h}_{ab} = (h_a + h_b)/2$, and index b refers to the neighbors of particle a . The divergence of this term results in the Laplacian of the kernel W . For most kernels used in SPH, this term is certainly not zero and therefore this should not be ignored. We investigate the importance of including these terms in section 4. We note that in the case of elastic dynamics that these terms are negligible and do not make a significant difference. This has also been pointed out by Zhang et al. [18].

The Jaumann stress rate is also similarly modified to account for the transport velocity as,

$$\frac{d\tilde{\sigma}'_{ij}}{dt} = 2G(\dot{\epsilon}_{ij} - \frac{1}{3}\dot{\epsilon}_{kk}\delta_{ij}) + \sigma'_{ik}\Omega_{jk} + \Omega_{ik}\sigma'_{kj} + \frac{\partial}{\partial x_k} (\sigma'_{ij}(\tilde{u}_k - u_k)) - \sigma'_{ij} \frac{\partial}{\partial x_k} (\tilde{u}_k - u_k). \quad (21)$$

3.1. The EDAC-SPH method

We apply the EDAC-SPH [21] in order to evolve the pressure accurately and reduce the amount of noise in the pressure field. In the original EDAC-SPH implementation, internal flows were evolved using the TVF whereas for cases with a free-surface the traditional WCSPH was employed. In this work we propose a unified approach by carefully incorporating free-surfaces. The original EDAC-SPH scheme also did not accurately incorporate the transport

velocity which we include here. This allows us to use the same scheme for both internal and external flows.

The δ -SPH [27] implementation is in principle similar to the EDAC-SPH method but requires the use of the kernel gradient corrections which involve the solution of a small matrix (3×3 in 3D), for each particle. The EDAC-SPH method does not require this and is therefore simpler and in principle more efficient. In [21], the EDAC pressure evolution equation was,

$$\frac{dp}{dt} = -\rho c_s^2 \text{div}(\mathbf{u}) + \nu_{edac} \nabla^2 p, \quad (22)$$

where ν_{edac} is a viscosity parameter for the smoothing of the pressure and c_s is the (artificial) speed of sound. We discuss this term later. However, in the context of the consistent evolution using the transport velocity, we note that the above should be evolved using,

$$\frac{\tilde{d}p}{dt} = (p - \rho c_s^2) \text{div}(\mathbf{u}) - p \text{div}(\tilde{\mathbf{u}}) + \text{div}(p(\tilde{\mathbf{u}} - \mathbf{u})) + \nu_{edac} \nabla^2 p. \quad (23)$$

The value of ν_{edac} is suggested as,

$$\nu_{edac} = \frac{\alpha_{edac} h c_s}{8}, \quad (24)$$

where h is the smoothing length of the kernel and a value of $\alpha_{edac} = 0.5$ is recommended.

This along with the momentum equation and evolution of volume or density may be employed. A state equation is often used even for elastic dynamics problems, we propose to use the EDAC approach for elastic equations as well as this reduces the amount of artificial viscosity that is needed.

3.2. SPH discretization

In the current work, both fluid and solid modelling uses the same continuity and pressure evolution equation. The SPH discretization of the continuity equation (12) and the pressure evolution equation (23) respectively are,

$$\frac{\tilde{d}\rho_a}{dt} = \sum_b \frac{m_b}{\rho_b} (\rho_a \tilde{\mathbf{u}}_{ab} + (\rho(\tilde{\mathbf{u}} - \mathbf{u}))_{ab}) \cdot \nabla_a W_{ab}, \quad (25)$$

$$\frac{d\tilde{p}_a}{dt} = \sum_b \frac{m_b}{\rho_b} \left((p_a - \rho_a c_s^2) \mathbf{u}_{ab} + p_a \tilde{\mathbf{u}}_{ab} - (p(\tilde{\mathbf{u}} - \mathbf{u}))_{ab} + 4\nu_{edac} \frac{p_a - p_b}{(\rho_a + \rho_b)(r_{ab}^2 + 0.01h_{ab}^2)} \mathbf{r}_{ab} \right) \cdot \nabla_a W_{ab}. \quad (26)$$

Similarly, the discretized momentum equation for fluids is written as,

$$\begin{aligned} \frac{d\tilde{\mathbf{u}}_a}{dt} = & - \sum_b m_b \left[\left(\frac{p_a}{\rho_a^2} + \frac{p_b}{\rho_b^2} \right) \mathbf{I} - \left(\frac{\mathbf{A}_a}{\rho_a^2} + \frac{\mathbf{A}_b}{\rho_b^2} + \Pi_{ab} \mathbf{I} \right) \right] \cdot \nabla_a W_{ab} \\ & + \mathbf{u}_a \sum_b \frac{m_b}{\rho_b} \tilde{\mathbf{u}}_{ab} \cdot \nabla_a W_{ab} + \sum_b m_b \frac{4\eta \nabla W_{ab} \cdot \mathbf{r}_{ab}}{(\rho_a + \rho_b)(r_{ab}^2 + 0.01h_{ab}^2)} \mathbf{u}_{ab} + \mathbf{g}_a, \end{aligned} \quad (27)$$

where $\mathbf{A}_a = \mathbf{u}_a \otimes (\tilde{\mathbf{u}}_a - \mathbf{u}_a)$, \mathbf{I} is the identity matrix, η is the kinematic viscosity of the fluid and Morris et al. [28] formulation is used to discretize the viscosity term. Π_{ab} is the artificial viscosity [3] to maintain the stability of the numerical scheme. It is given as,

$$\Pi_{ab} = \begin{cases} \frac{-\alpha h_{ab} \bar{c}_{ab} \phi_{ab}}{\bar{\rho}_{ab}} & \mathbf{u}_{ab} \cdot \mathbf{r}_{ab} < 0, \\ 0 & \mathbf{u}_{ab} \cdot \mathbf{r}_{ab} \geq 0, \end{cases} \quad (28)$$

where,

$$\phi_{ab} = \frac{\mathbf{u}_{ab} \cdot \mathbf{r}_{ab}}{r_{ab}^2 + 0.01h_{ab}^2}, \quad (29)$$

where $\mathbf{r}_{ab} = \mathbf{r}_a - \mathbf{r}_b$, $\mathbf{u}_{ab} = \mathbf{u}_a - \mathbf{u}_b$, $h_{ab} = (h_a + h_b)/2$, $\bar{\rho}_{ab} = (\rho_a + \rho_b)/2$, $\bar{c}_{ab} = (c_a + c_b)/2$, and α is the artificial viscosity parameter.

For solid mechanics the momentum equation is written as,

$$\frac{d\tilde{\mathbf{u}}_a}{dt} = - \sum_b m_b \left[\left(\frac{p_a}{\rho_a^2} + \frac{p_b}{\rho_b^2} \right) \mathbf{I} - \left(\frac{\boldsymbol{\sigma}'_a}{\rho_a^2} + \frac{\boldsymbol{\sigma}'_b}{\rho_b^2} + \Pi_{ab} \mathbf{I} \right) \right] \cdot \nabla_a W_{ab} + \mathbf{g}_a, \quad (30)$$

we have not considered the correction stress term \mathbf{A} in momentum equation of solid mechanics as it has a negligible effect.

In addition to these three equations, the Jaumann stress rate equation is also solved. In the current work we use the momentum velocity \mathbf{u} rather

than $\tilde{\mathbf{u}}$ as in the GTVF [18] in the computation of gradient of velocity. The SPH discretization of the gradient of velocity is given as,

$$\nabla \mathbf{u}_a = - \sum_b \frac{m_b}{\rho_b} (\mathbf{u}_a - \mathbf{u}_b) \otimes (\nabla_a W_{ab}), \quad (31)$$

where \otimes is the outer product.

The SPH discretization of the modified Jaumann stress rate eq. (21) is given as,

$$\begin{aligned} \frac{d\tilde{\boldsymbol{\sigma}}'_a}{dt} = & 2G(\dot{\boldsymbol{\epsilon}}_a - \frac{1}{3}\dot{\boldsymbol{\epsilon}}_a \mathbf{I}) + \boldsymbol{\sigma}'_a \boldsymbol{\Omega}_a^T + \boldsymbol{\Omega}_a \boldsymbol{\sigma}'_a + \\ & + \sum_b \frac{m_b}{\rho_b} (\boldsymbol{\sigma}' \otimes (\tilde{\mathbf{u}} - \mathbf{u}))_{ab} \cdot \nabla_a W_{ab} + \boldsymbol{\sigma}'_a \sum_b \frac{m_b}{\rho_b} (\tilde{\mathbf{u}} - \mathbf{u})_{ab} \cdot \nabla_a W_{ab}. \end{aligned} \quad (32)$$

3.3. Particle transport

The particles in the current scheme are moved with the transport velocity,

$$\frac{d\mathbf{r}_a}{dt} = \tilde{\mathbf{u}}_a. \quad (33)$$

The transport velocity is updated using,

$$\tilde{\mathbf{u}}_a(t + \Delta t) = \mathbf{u}_a(t) + \Delta t \frac{d\tilde{\mathbf{u}}_a}{dt} + \left(\frac{d\mathbf{u}_a}{dt} \right)_c \Delta t \quad (34)$$

Where $\left(\frac{d\mathbf{u}_a}{dt} \right)_c$ is the homogenization acceleration computed as described in section 3.3.1 and section 3.3.2. This acceleration ensures that the particle positions are homogeneous.

3.3.1. Sun 2019 PST

In Sun et al. [29], the particle shifting technique was implemented as a particle displacement ($\delta \mathbf{r}$). This was modified in Sun et al. [20] to be computed as a change to the velocity. In the present work we modify this to be treated as an acceleration to the particle in order to unify the treatment of different PST methods.

Firstly, the velocity deviation based equation is given as,

$$\delta \mathbf{u}_a = -\text{Ma} (2h)c_0 \sum_b \left[1 + R \left(\frac{W_{ab}}{W(\Delta x)} \right)^n \right] \nabla_a W_{ab} V_b, \quad (35)$$

it is modified to force based as,

$$\left(\frac{d\mathbf{u}_a}{dt}\right)_c = -\frac{\text{Ma} (2h)c_0}{\Delta t} \sum_b \left[1 + R\left(\frac{W_{ab}}{W(\Delta x)}\right)^n\right] \nabla_a W_{ab} V_b, \quad (36)$$

where R is an adjustment factor to handle the tensile instability, and Ma is the mach number of the flow. V_b is the volume of the b^{th} particle. The acceleration is changed to account for particles that are on the free surface. We use $R = 0.2$ and $n = 4$.

3.3.2. IPST

The Iterative PST of Huang [15] builds on the work of Xu et al. [30]. The method iteratively moves the particles every timestep in order to achieve a uniform particle distribution determined by a convergence criterion. The properties of the particles are corrected using a Taylor series expansion.

In the original IPST, the shifting vector is computed as,

$$\delta r_a^m = U_{\max} \Delta t \sum_b (V_b \mathbf{n}_{ab} W_{ab})^m, \quad (37)$$

where m is the number of iterations, $m = (1, 2, 3, \dots)$. The particles are then moved using this displacement using,

$$\mathbf{r}_a^{m+1} = \mathbf{r}_a^m + \delta \mathbf{r}_a^m. \quad (38)$$

This is repeated until the convergence criterion is achieved. The convergence criterion is defined as

$$|\max(\chi_a^m) - \overline{\chi_a^m}| \leq \epsilon, \quad (39)$$

where

$$\chi_a^m = h^2 \sum W_{ab}^m, \quad (40)$$

and $\overline{\chi_a^m}$ is the value of χ_a^m computed with the initial configuration of the particles. For problems where there is no free surface this value is a constant computed using the initial configuration. For free-surface problems it is computed as the maximum value of χ_a^m at the initial configuration, which corresponds to the a free surface particle.

The initial and final positions of the particles are used to determine an acceleration on the particle that would produce such a displacement. This is computed as

$$\left(\frac{d\mathbf{u}_a}{dt}\right)_c = 2 \frac{\mathbf{r}_a^M - \mathbf{r}_a^0}{\Delta t^2}, \quad (41)$$

where \mathbf{r}_a^M is the final position of the particle, a .

3.4. Free surface identification algorithm

Free surfaces must be handled with care especially in the context of the PST algorithm. The original TVF [17] is not designed to handle free-surface problems. Lind et al. [13] was the first to handle free-surfaces carefully in the context of the PST. Lind et al. [13], Oger et al. [19], and Sun et al. [20] identify the particles that are on the free-surface or near it and adjust the particle shifting algorithm so the free surface particles remain intact. Zhang et al. [18] on the other hand relies on the pressure being zero at the free surface and scales the homogenization force with the pressure.

Both [19] and [20] identify the free-surface particles by computing the eigenvalues of the correction matrix employed for the SPH scheme. This is based on the work of [31]. This method is computationally expensive and in this work we use a much simpler approach that was introduced in [32] to find the free-surface particles as well as their normals. We first compute the normals of all the particles in the medium whose free surface need to be identified. The normals are computed as,

$$\mathbf{n}_a^* = \sum_b -\frac{m_b}{\rho_b} \nabla_a W_{ab} \quad (42)$$

If the magnitude of the resulting vector is less than $\frac{1}{4h_a}$, then the \mathbf{n}^* is set to zero otherwise we normalize the vector by its magnitude. Then, we smooth these normals using an SPH approximation,

$$\hat{\mathbf{n}}_a = \sum_b \frac{m_b}{\rho_b} \mathbf{n}_b^* W_{ab}. \quad (43)$$

Finally, we normalize $\hat{\mathbf{n}}_a$ so they are unit vectors. We note that for particles that are isolated and have no neighbors the above algorithm will not work. We identify all such particles by computing the summation density of all particles and any particles with a summation density that is lower than half the fluid density are marked as free-surface particles. For the quintic spline kernel used in this work we find that the cutoff value of half the fluid density is effective in differentiating particles that are away from the bulk fluid.

As can be seen from fig. 1, three layers of particles which are near the free surface have a normal. From these normals we need to find the surface particles. We loop over all the particles in the medium, and any particles which have a non-zero normal are considered for further analysis. For each of these potential surface particles we find the angle between the particle and

each of its neighbors. If the angle between the normal of the particle and that of the line joining the particle to its neighbor is less than 60 degrees then this particle is *not* considered as a free-surface particle. If no such neighbor exists, then the particle is considered to be a free-surface particle. As can be seen in fig. 2, the free surface particles are properly identified. This process is both accurate for a variety of test cases and computationally efficient.

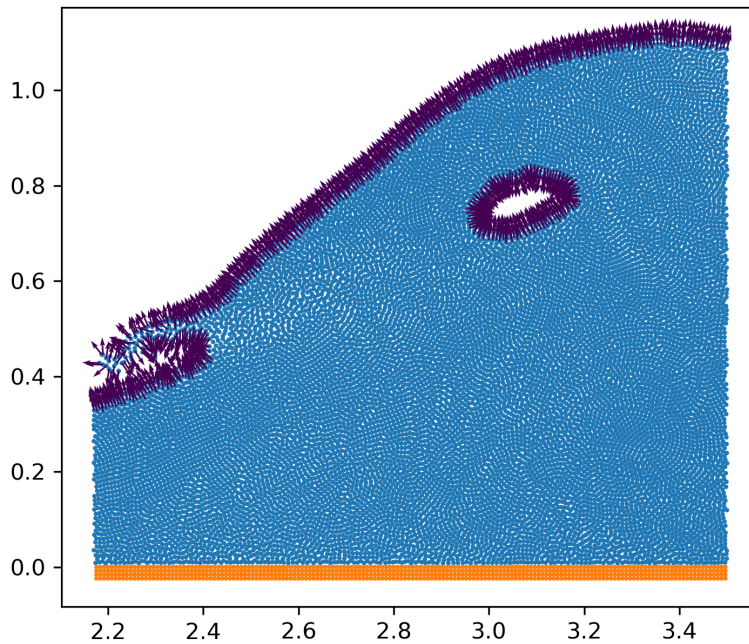


Figure 1: Identification of normals of fluid in a dam break simulation. Shows us the normals of all the fluid particles

3.5. *PST close to the free surface*

Near the free-surface the PST has to be performed with some care for both fluids and solids. This is because of the lack of support for the particles near the free-surface. After the free surface particles are identified by using the algorithm described in section 3.4, we mark the particles which are in

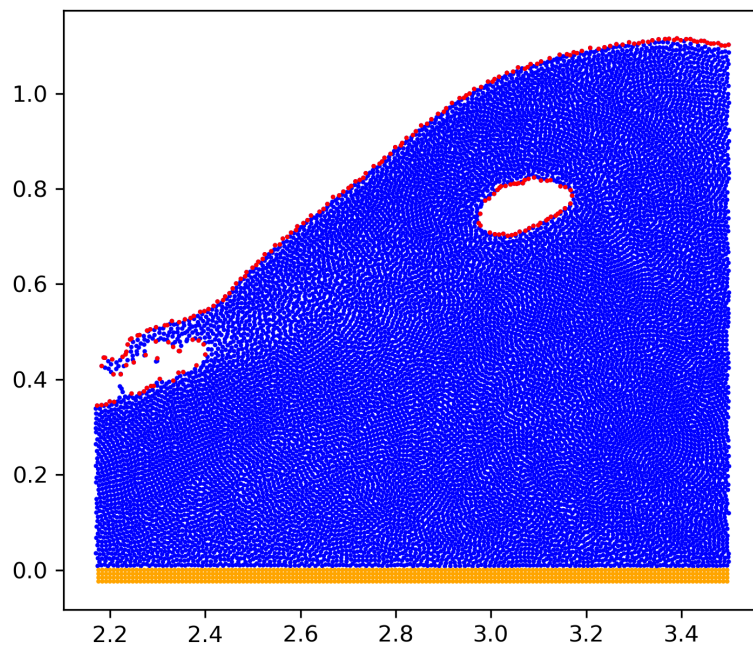


Figure 2: Identification of boundary particles of fluid at an instance in a dam break. Shows boundary particles of all the fluid particles

close proximity to the free surface particles. This is done through a variable associated with each particle called h_b , which is initialized to the initial smoothing length of the particles.

We loop over all the particles that are not on the boundary, and their h_b is adjusted to the distance to the closest boundary particle divided appropriately by a kernel-dependent factor such that the kernel support is up to the closest boundary particle. In the current work, we have used a quintic spline kernel for which the factor is 3. The algorithm is shown in algorithm 1 and depicted in fig. 3. We note that this h_b is only used for the PST force/displacement computation. This process allows us to ensure that the homogenization force does not push these particles towards the free-surface.

Algorithm 1 Algorithm to set h_b

```

1: for particle  $i$  in all particles do
2:   if  $i$  is a boundary particle then
3:     set  $h_{b,i} = 0$ 
4:   else
5:     set  $h_{b,i} = h$ 
6: for particle  $i$  in all non-boundary particles do
7:   if particle  $i$  has a boundary particle in its neighborhood then
8:      $x_{\text{dist},i} \leftarrow$  Distance to nearest boundary particle
9:     Set  $h_{b,i} = \frac{x_{\text{dist},i}}{3}$ 

```

In the PST of Sun et al. [20], the shifting acceleration is adjusted using

$$\left(\frac{d\mathbf{u}_a}{dt}\right)_c = \begin{cases} 0 & \text{if boundary,} \\ \left(\frac{d\mathbf{u}_a}{dt}\right)_c - \left(\left(\frac{d\mathbf{u}_a}{dt}\right)_c \cdot \mathbf{n}_a\right)\mathbf{n}_a & \text{if } h_b < h, \\ \left(\frac{d\mathbf{u}_a}{dt}\right)_c & \text{if } h_b = h. \end{cases} \quad (44)$$

Whereas while using IPST [15], rather than adjusting the final shifting acceleration, we adjust the increment in the position of eq. (38),

$$\delta\mathbf{r}_a^m = \begin{cases} 0 & \text{if boundary,} \\ \delta\mathbf{r}_a^m - (\delta\mathbf{r}_a^m \cdot \mathbf{n}_a)\mathbf{n}_a & \text{if } h_b < h, \\ \delta\mathbf{r}_a^m & \text{if } h_b = h. \end{cases} \quad (45)$$

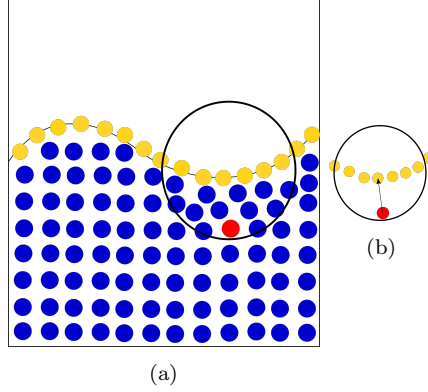


Figure 3: Set h_b of the particles. (a) Particles with a free surface whose free particles are identified (b) Minimum distance between the particle in the vicinity of the free surface to the free surface particle.

3.6. Boundary conditions

The ghost particle approach of Adami et al. [33] is used to model the boundaries. We use three layers of ghost particles to model the solid wall. The properties of the solid wall are interpolated from the fluid particles.

When computing the divergence of the velocity field on fluid particles, we enforce a no-penetration boundary condition and not a no-slip boundary condition. The velocity of the fluid is projected onto the ghost particles using,

$$\hat{\mathbf{u}}_a = \frac{\sum_b \mathbf{u}_b W_{ab}}{\sum_b W_{ab}}, \quad (46)$$

$$\tilde{\mathbf{u}}_a = \frac{\sum_b \tilde{\mathbf{u}}_b W_{ab}}{\sum_b W_{ab}}, \quad (47)$$

where \mathbf{u}_b , $\tilde{\mathbf{u}}_b$ are the momentum and transport velocity of the fluid respectively and W_{ab} is the kernel value between the fluid particle and the ghost particle.

The normal component of this projected velocity is then reflected and set as the ghost particle velocity,

$$\mathbf{u}_{\text{Ga}} = 2\hat{\mathbf{n}}((\mathbf{u}_p - \hat{\mathbf{u}}_a) \cdot \hat{\mathbf{n}}) + \hat{\mathbf{u}}_a, \quad (48)$$

where \mathbf{u}_p is the local velocity of the boundary and $\hat{\mathbf{n}}$ is the unit normal to the boundary particle a . Similarly the transport velocity of the ghost particle is

set as,

$$\tilde{\mathbf{u}}_{Gi} = 2\hat{\mathbf{n}}((\mathbf{u}_p - \tilde{\mathbf{u}}_i) \cdot \hat{\mathbf{n}}) + \tilde{\mathbf{u}}_i, \quad (49)$$

When the viscous force is computed, the no slip boundary condition is used, where the velocity on the boundary set as,

$$\mathbf{u}_{Ga} = 2\mathbf{u}_p - \hat{\mathbf{u}}_a, \quad (50)$$

a similar form is used for the transport velocity here too,

$$\tilde{\mathbf{u}}_{Ga} = 2\mathbf{u}_p - \tilde{\mathbf{u}}_a. \quad (51)$$

The pressure of the boundary particle is extrapolated from its surrounding fluid particles by the following equation,

$$p_w = \frac{\sum_f p_f W_{wf} + (\mathbf{g} - \mathbf{a}_w) \cdot \sum_f \rho_f \mathbf{r}_{wf} W_{wf}}{\sum_f W_{wf}}, \quad (52)$$

where \mathbf{a}_w is the acceleration of the wall. The subscript f denotes the fluid particles and w denotes the wall particles.

For solid mechanics problems, in addition to the extrapolation of pressure, we also extrapolate the deviatoric shear stress on to the boundary particles using,

$$\sigma'_{ij} = \frac{\sum_s \sigma'_{ij} W_{ws}}{\sum_s W_{ws}}, \quad (53)$$

where s denotes the solid particles.

3.7. Time integration

We use the kick-drift-kick scheme for the time integration. We first move the velocities of the particles to half time step,

$$\mathbf{u}_a^{n+\frac{1}{2}} = \mathbf{u}_a^n + \frac{\Delta t}{2} \left(\frac{d\tilde{\mathbf{u}}_a}{dt} \right)^n, \quad (54)$$

$$\tilde{\mathbf{u}}_a^{n+\frac{1}{2}} = \mathbf{u}_a^{n+\frac{1}{2}} + \frac{\Delta t}{2} \left(\frac{d\mathbf{u}_a}{dt} \right)_c^n. \quad (55)$$

Then the time derivatives of density and deviatoric stresses are calculated using the eq. (25) and eq. (4). The new time step density, deviatoric stresses and particle position are updated by,

$$\rho_a^{n+1} = \rho_a^n + \Delta t \left(\frac{d\tilde{\rho}_a}{dt} \right)^{n+\frac{1}{2}}, \quad (56)$$

$$p_a^{n+1} = p_a^n + \Delta t \left(\frac{\tilde{d}p_a}{dt} \right)^{n+\frac{1}{2}}, \quad (57)$$

$$\boldsymbol{\sigma}'_a{}^{n+1} = \boldsymbol{\sigma}'_a{}^n + \Delta t \left(\frac{\tilde{d}\boldsymbol{\sigma}'_a}{dt} \right)^{n+\frac{1}{2}}, \quad (58)$$

$$\mathbf{r}_a^{n+1} = \mathbf{r}_a^n + \Delta t \tilde{\mathbf{u}}_a^{n+1}. \quad (59)$$

Finally, at new time-step particle position, the momentum velocity is updated

$$\mathbf{u}_a^{n+1} = \mathbf{u}_a^{n+\frac{1}{2}} + \frac{\Delta t}{2} \left(\frac{\tilde{d}\mathbf{u}_a}{dt} \right)^{n+1}. \quad (60)$$

For the numerical stability, the time step depends on the CFL condition as,

$$\Delta t = \min \left(0.25 \frac{h}{c + |U|}, 0.25 \frac{h^2}{\nu}, 0.25 \frac{h^2}{g} \right), \quad (61)$$

where $|U|$ is the maximum velocity magnitude, c is the speed of sound typically chosen as $10|U|$ for fluids in this work.

For solid mechanics, the timestep is set based on the following,

$$\Delta t \leq 0.25 \left(\frac{h}{c_0 + |U|} \right), \quad (62)$$

where c_0 is the speed of sound of the solid body.

4. Results

We validate the proposed scheme using a suite of benchmark problems for both fluid and solid mechanics. We first consider fluids where we look at the Taylor-Green vortex problem, the lid-driven cavity, and the two-dimensional dam-break problem. We then consider problems in elastic dynamics like the oscillating plate, a uniaxial compression problem, the collision of rubber rings, and a high-velocity impact problem.

We show how the proposed method is an improvement on previous work. Every result shown is produced using an automation framework [26]. The source code is available at <https://gitlab.com/pypr/ctvf>.

4.1. Taylor-Green vortex

The Taylor-Green vortex problem features an exact solution with which we can study the accuracy of our proposed method. The problem consists of a periodic unit box with no solid boundaries. The exact solution is given as,

$$u = -Ue^{bt} \cos(2\pi x) \sin(2\pi y) \quad (63)$$

$$v = Ue^{bt} \sin(2\pi x) \cos(2\pi y) \quad (64)$$

$$p = -U^2 e^{2bt} (\cos(4\pi x) + \cos(4\pi y))/4, \quad (65)$$

where U is chosen as 1ms^{-1} , $b = -8\pi^2/Re$, $Re = UL/\nu$, and $L = 1\text{m}$. We initialize the fluid using this at $t = 0$ and compare the results with the exact solution. The Reynolds number, Re , is initially chosen to be 100. The quintic spline with $h/\Delta x = 1.0$ is used. We use summation density to compute the density and evolve pressure with eq. (26). No artificial viscosity is used for this problem. The decay rate of the velocity is studied using the evolution of maximum velocity $|\mathbf{u}_{\max}|$ in time. We compute the L_1 error in the velocity magnitude as,

$$L_1 = \frac{\sum_i |\mathbf{u}_{i,\text{computed}}| - |\mathbf{u}_{i,\text{exact}}|}{\sum_i |\mathbf{u}_{i,\text{exact}}|}, \quad (66)$$

where $\mathbf{u}_{i,\text{exact}}$ is found at the position of the i 'th particle.

In fig. 4a we compare the decay of the maximum speed with that of the exact solution for the case where we use the PST of Sun et al. [20]. As can be seen the results are in excellent agreement with the expected decay. The same is seen in fig. 5a for the case using the IPST technique of Huang et al. [15]. This shows the accuracy of the scheme and robustness to changing the PST method used. Figure 4b and fig. 5b show the L_1 error of velocity magnitude for various resolutions simulated using the two different PST techniques.

One can see that the IPST method has lower errors at initial times. However, we do note that there appears to be a lack of convergence in the result as the resolution is increased. As the number of particles is increased the L_1 error does not correspondingly reduce. This is due to the low Reynolds number and the discretization of the viscous term that is being used. We show the results of the velocity decay and the L_1 error when a Reynolds number of 1000 is used in fig. 6 for the IPST and in fig. 7 with Sun's method. In this case the convergence is clearly seen as the resolution is increased.

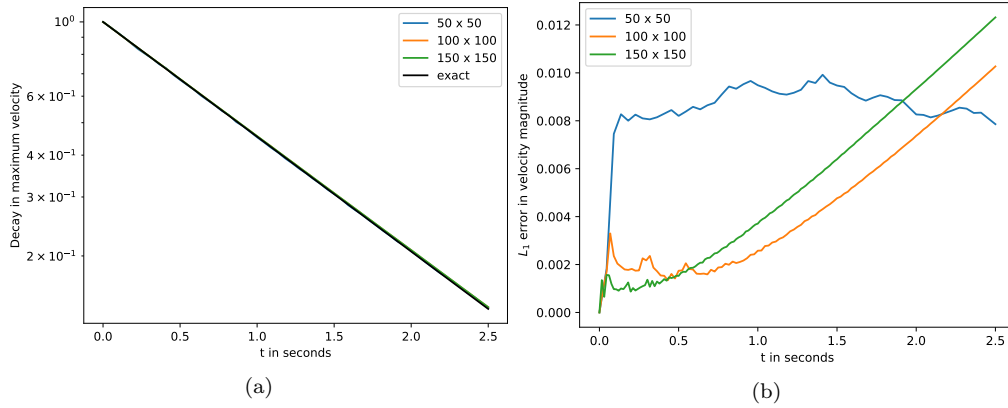


Figure 4: Taylor-Green vortices for an initial particle distribution of 50×50 , 100×100 and 150×150 is simulated with a Reynolds number of 100 using Sun 2019 technique. Plots shown are (a) decay in maximum velocity (b) L_1 error in velocity magnitude.

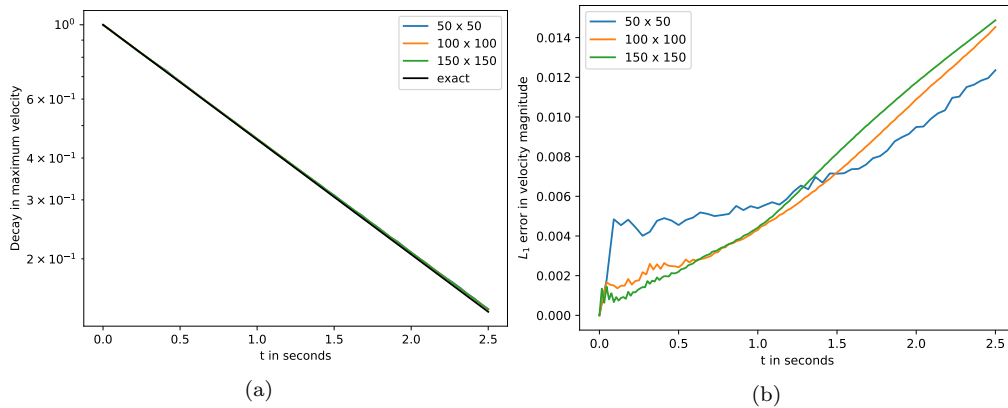


Figure 5: Taylor-Green vortices for an initial particle distribution of 50×50 , 100×100 and 150×150 is simulated with a Reynolds number of 100 using IPST technique. Plots shown are (a) decay in maximum velocity (b) L_1 error in velocity magnitude.

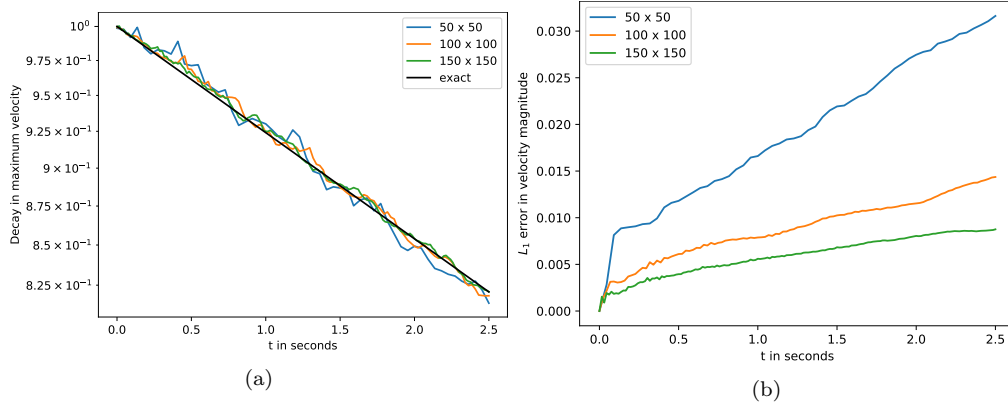


Figure 6: Taylor-Green vortices for an initial particle distribution of 50×50 , 100×100 and 150×150 is simulated with a Reynolds number of 1000 using IPST technique. Plots shown are (a) decay in maximum velocity (b) L_1 error in velocity magnitude.

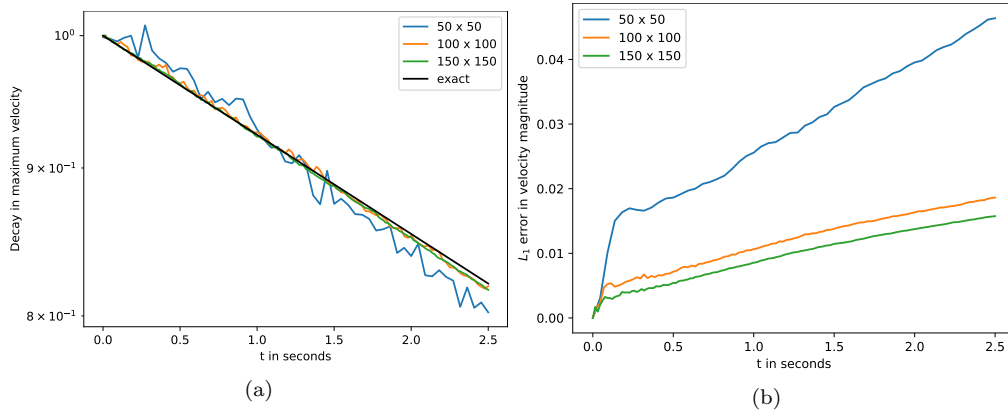


Figure 7: Taylor-Green vortices for an initial particle distribution of 50×50 , 100×100 and 150×150 is simulated with a Reynolds number of 1000 using Sun 2019 technique. Plots shown are (a) decay in maximum velocity (b) L_1 error in velocity magnitude.

4.2. Lid driven cavity

The lid-driven cavity is a classic problem that can be challenging to simulate in the context of the SPH. It has been simulated by [17], [15], [21] to note a few. A rectangular cavity with length 1 m which is filled with fluid is constrained by four walls. Top wall has a velocity of $U = 1\text{ms}^{-1}$. We simulate problem for both $Re = 100$ and 1000. A unit density is assumed for the fluid. The speed of sound of the fluid particle is set to $c = 10U_{max}$. We use the summation density to compute the density at each instant of the simulation. The viscosity of the fluid is set through the Reynolds number of the flow, $\nu = \frac{Re}{U}$. No artificial viscosity is used in the current problem. Figure 8 and fig. 9 show the center-line velocities u versus y and v versus x for the Reynolds numbers 100 and 1000 respectively. For the $Re = 100$ case we use three different resolutions of 50×50 , 100×100 and 150×150 . For the $Re = 1000$ case, we use an initial 50×50 , 100×100 , and 200×200 grid of particles. These are compared against the results of [34]. As we can see that the current scheme is able to predict the velocity profiles well.

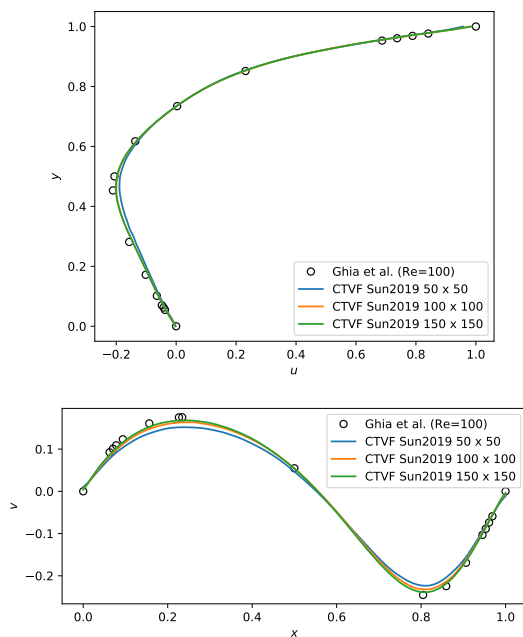


Figure 8: Velocity profiles u vs. y and v vs. x for the lid-driven-cavity problem at $Re = 100$ with three initial particle arrangement of 50×50 , 100×100 , and 150×150 .

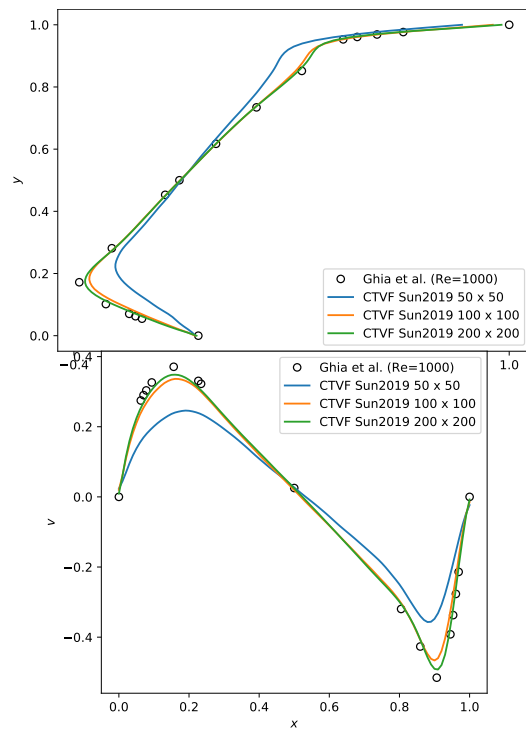


Figure 9: Velocity profiles for the lid-driven-cavity using the steady state simulation procedure for $Re = 1000$ with initial partial arrangement of 50×50 , 100×100 , and 200×200 compared with the results of [34].

4.3. 2D Dam-break

In this benchmark we test the ability of the current scheme to simulate free surface flows. This problem has been extensively studied before for example in [32], [18], and [21].

A block of fluid having width 1m and a height of 2m is allowed to settle under the influence of gravity inside a tank of length 4m. The fluid block is initially placed to the left of the tank. The acceleration due to gravity is $g = 9.81\text{ms}^{-1}$. To simulate the free surface flows we use the continuity equation to evolve the density using (25) and the (26) to evolve the pressure. We use free slip boundary conditions to compute the divergence of the velocities and a no-slip boundary condition while computing the viscous forces. The value of $\alpha = 0.05$ is used for the artificial viscosity eq. (28) term.

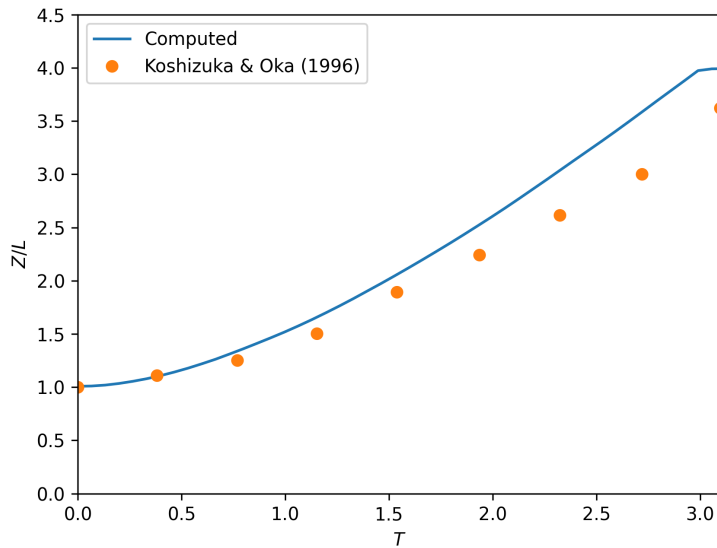


Figure 10: Position of the toe of the water versus time of CTVF as compared with the simulation of [35]. Z is the distance of toe of the dam from the left wall and L is the initial width of the dam

Figure 10 compares the position of the toe of the fluid block with time against [35], where the authors use the moving particle semi-implicit scheme to simulate the same.

The evolution of the fluid at three different time instants $t = 0.6, 1.1, 2.0$ seconds, is shown in fig. 11. As can be seen from fig. 11, at time 2.0 seconds we

have captured the void created due to the splashing of the fluid. The colors in fig. 11 represent the pressure and fig. 12 shows the velocity magnitude.

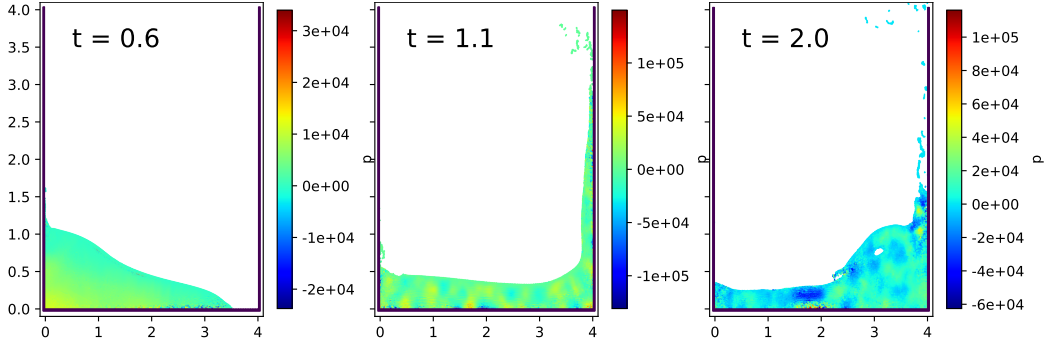


Figure 11: Particle plots of fluid in dam break at times $t = 0.6, 1.1, 2.0$ seconds, showing pressure as contour.

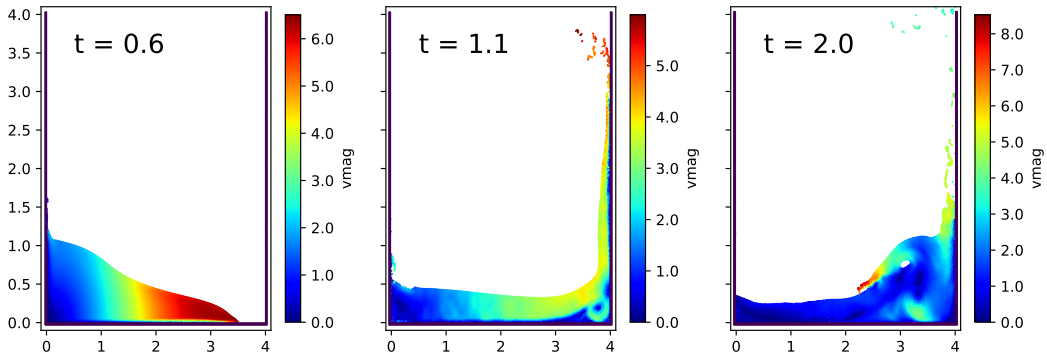


Figure 12: Particle plots of fluid in dam break at time $t = 0.6, 1.1, 2.0$ second, showing velocity magnitude as contour.

4.4. Oscillating plate

In this benchmark we simulate the oscillation of a thin plate which is clamped on one side. Landau et al. [36] provide an analytical solution for this problem. This is also simulated numerically in [7] and [18].

An oscillating plate with a length of 0.2m and a height of 0.02m is initially given with a velocity profile of,

$$v_y(x) = V_f c_0 \frac{F(x)}{F(L)},$$

where V_f varies for different cases. L is the length of the plate. $F(x)$ is given by,

$$F(x) = (\cos(kL) + \cosh(kL)) (\cosh(kx) - \cos(kx)) + (\sin(kL) - \sinh(kL)) (\sinh(kx) - \sin(kx)). \quad (67)$$

In the present example kL is 1.875. The material properties of the plate are as follows, Young's modulus $E = 2.0 \times 10^6 \text{Pa}$, a Poisson's ratio of $\nu = 0.3975$. c_0 is speed of sound, and a density of $\rho = 1000 \text{kgm}^{-3}$. In all the cases simulated here, we use an α of 1 for artificial viscosity.

Here we show the inability of the GTVF [18] scheme to eliminate numerical fracture scheme when Sun's PST [29] rather than the one originally proposed in their work. We use a particle spacing of $\Delta x = 0.002 \text{m}$ and run the simulation using the GTVF scheme [18], with $V_f = 0.05 \text{ms}^{-1}$. Instead of using the standard GTVF homogenization acceleration we use Sun's particle shifting technique. This results in a numerical fracture, as seen in fig. 13. This numerical fracture is eliminated by the current scheme. This is due to the incorporation of the additional terms in continuity equation (12) as well as the usage of momentum velocity in velocity gradient computation.

This is further demonstrated by a case where an oscillating plate of length of 0.2m and a height of 0.02m is simulated for a time of 0.22 seconds. Similarly, another case where plate of height 0.01m and a width of 0.2m is run for a time of 0.51s. Figure 14 and fig. 15 shows particles of the plate at time $t = 0.22 \text{s}$ and 0.51s of these two cases respectively. As we can see from the figure that the plate is free of numerical fracture, thus the tensile instability is eliminated.

The accuracy of the current scheme is evaluated by comparing with the analytical results and with a convergence study. In table 1 we compare the time period for the oscillation by the analytical and the numerical results with varying V_f , where we consider an oscillating plate whose H/L ratio is 0.1. In fig. 16, we have performed a convergence study of an oscillating plate, with a $\nu = 0.3975$, and $V_f = 0.05 \text{ms}^{-1}$, and the IPST technique is used. As can be seen the proposed method performs very well.

4.5. Uniaxial compression

This benchmark is used to test the proposed scheme. A uniaxial bar is compressed by a moving piston on top of it. This problem has been simulated

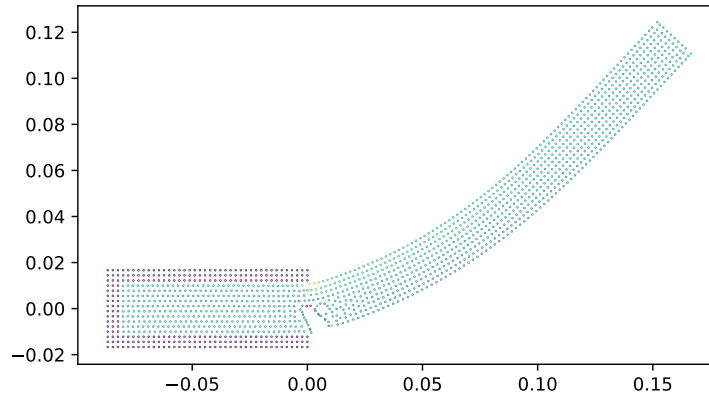


Figure 13: Numerical fracture of an oscillating plate with a length of 0.2m and height of 0.02m when simulated with Sun 2019 PST with GTVF scheme.

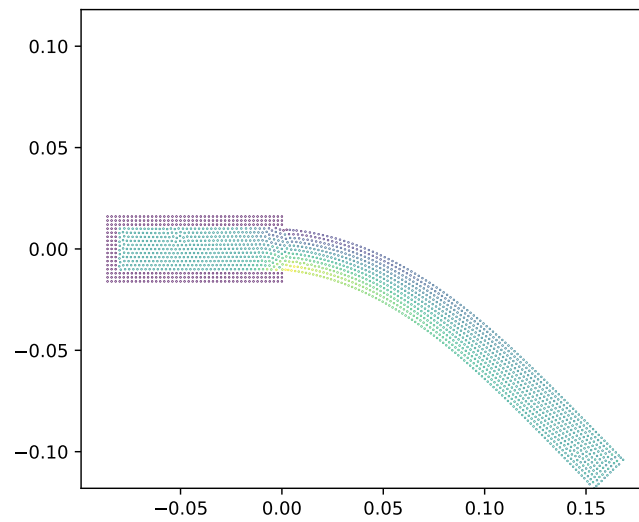


Figure 14: Oscillating plate at time $t = 0.22s$ with a length of 0.2m and height of 0.02m simulated with Sun 2019 PST with CTVF scheme.

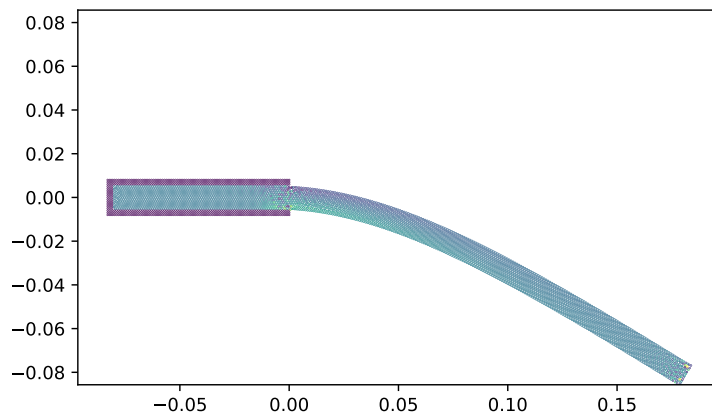


Figure 15: Oscillating plate at time $t = 0.51s$ with a length of 0.2m and height of 0.01m simulated with Sun 2019 PST with CTVF scheme.

V_f	0.001	0.01	0.03	0.05
T_{CTVF}	0.284	0.283	0.283	0.284
T_{GTVF}	0.284	0.283	0.284	0.285
$T_{analytical}$	0.254	0.252	0.254	0.254

Table 1: Comparison between the CTVF and the analytical solution for the time period of the oscillating plate with a length of 0.2m and height of 0.02m with various V_f

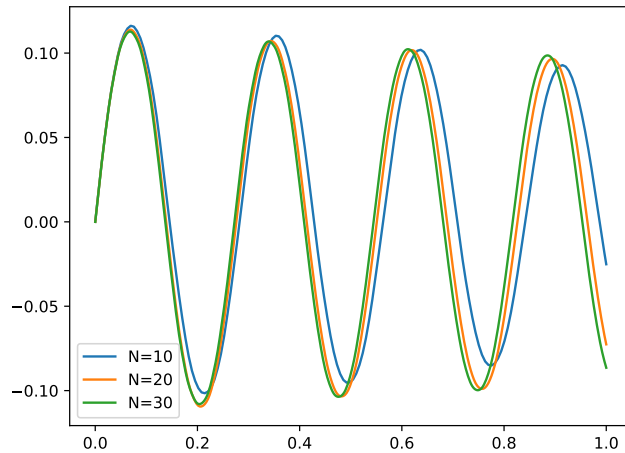


Figure 16: The vertical position of the particle at the end of the plate as a function of time. Here we consider a three particle variations, 10, 20 and 30 particles across the plate width.

by Das and Cleary [37]. We compare the von Mises stress at the center point of the bar with the result of the FEM analysis and SPH provided in [37].

The numerical model consists of three parts. It has an axially loaded rectangular specimen of width 82 mm and height of 140 mm. The specimen has the properties of a sand stone (Crossley Sandstone) with a Young's modulus of 7.5GPa and Poisson ratio of 0.398 and with a density of 2300 kgm^{-3} . The length and height of the specimen are as follows $82 \times 10^{-3}\text{m}$, $140 \times 10^{-3}\text{m}$. The speed of sound resulting from such properties is 2303ms^{-1} . We run three particle resolutions, $\Delta x = 0.5\text{mm}$, 1mm and 2mm. The particles are placed on a regular square grid pattern. The velocity of the top plate is 1.5mms^{-1} , which is used to apply the load on the specimen in such a fashion, such that the loaded end is deformed at the required constant rate. This is described in fig. 17. An α of 1 is used in the current simulation for the artificial viscosity.

We use the von Mises stress as the criterion for analysing the stress field. It combines the normal and shear components of the deviatoric stress tensor, and is a commonly used criterion to assess failure strength of materials. The von Mises stress σ_{vm} can be expressed in 2D in terms of principle stress σ_1

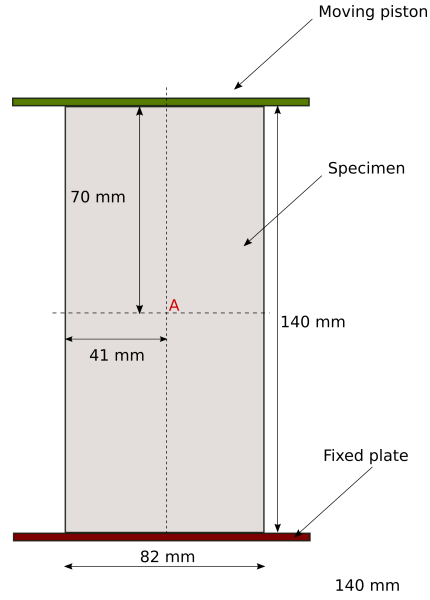


Figure 17: Test configuration of sand stone under uniaxial compression.

and σ_2 as

$$\sigma_{vm} = \sqrt{(\sigma_1^2 + \sigma_2^2 - \sigma_1 \sigma_2)} \quad (68)$$

Where the principal stress are found by

$$\sigma_1 = \frac{\sigma_{xx} + \sigma_{yy}}{2} + \sqrt{\left(\left(\frac{\sigma_{xx} + \sigma_{yy}}{2} \right)^2 + \sigma_{xy}^2 \right)} \quad (69)$$

$$\sigma_2 = \frac{\sigma_{xx} + \sigma_{yy}}{2} - \sqrt{\left(\left(\frac{\sigma_{xx} + \sigma_{yy}}{2} \right)^2 + \sigma_{xy}^2 \right)} \quad (70)$$

Figure 18 shows the von Mises stress versus time of the current scheme, when simulated with three different resolutions compared against with the finite element result and SPH result provided in [37]. It also shows the result with the GTVF scheme using the medium resolution. As can be seen in fig. 18 the GTVF result does not match very well with FEM and SPH result provided by Das and Cleary [37], and the current scheme performs significantly better.

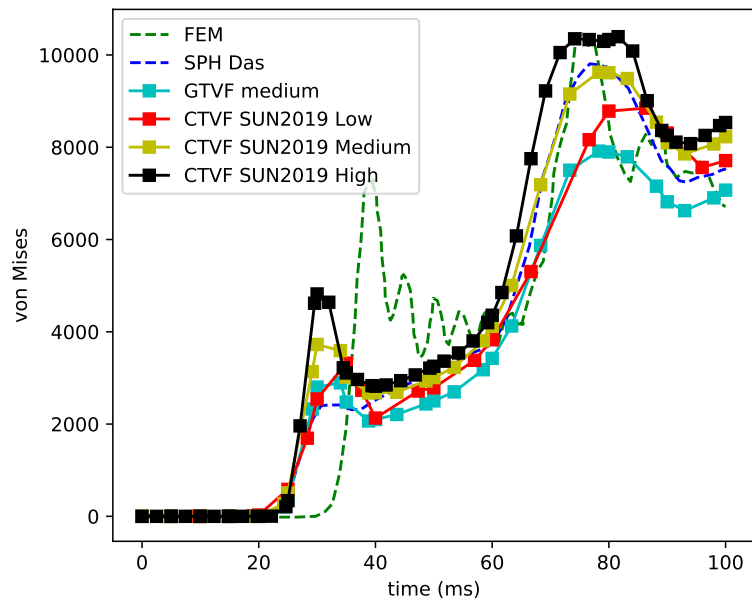


Figure 18: von Mises stress at point A in uniaxial compression with three different resolutions compared against those from [37].

4.6. Colliding Rings

In this example we investigate the collision of two rubber rings. This was initially done by Sweigle et al. [38]. The problem may display numerical fracture without the use of suitable corrections.

The inner ring radius of the ring is $r_{min} = 0.03\text{m}$ and the outer ring radius $r_{max} = 0.04\text{m}$. Both the rings have the same material properties: Young's modulus $E = 0.01\text{GPa}$ and density $\rho = 1.2 \times 10^3 \text{kgm}^{-3}$. The initial speed of the rings are equal to $v_0 = 0.12c_0\text{ms}^{-1}$ with an initial inter particle spacing of $\Delta x = 0.001\text{m}$. Where c_0 is the speed of sound of the material. We use an $\alpha = 1$ for the artificial viscosity in the current simulation, to add the artificial viscosity in stabilizing the scheme.

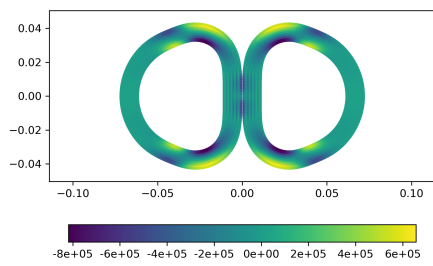
Two different Poisson ratios are simulated. Figure 19 shows the particle positions of rings with a Poisson ratio of 0.3975 when simulated with Sun's particle shifting technique.

We also consider higher Poisson ratios, such as 0.47. Figure 20 shows the particle positions of rings when simulated with Sun's PST and fig. 21 with IPST. Even though both the particle shifting techniques are able to eliminate the numerical fracture, IPST gives better results as in the distribution of particles through out the simulation, see fig. 20b and fig. 21b. For the case where Sun's PST is used, the final particle distribution is not very uniform. This is not the case for the IPST. In order to compare the different schemes quantitatively for this problem, we plot the x and y positions of the point A of the left ring, as can be seen in fig. 22. Figure 23 shows the results and as can be seen excellent agreement of the different methods for this problem.

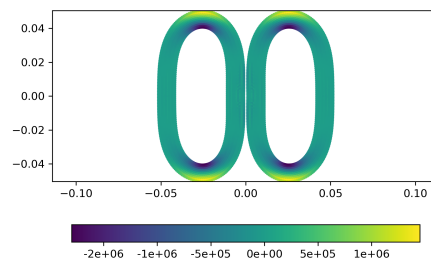
4.7. High velocity impact

High-velocity impact problems are important in various contexts like space debris applications. This case tests if the scheme is capable of hand large deformation problems.

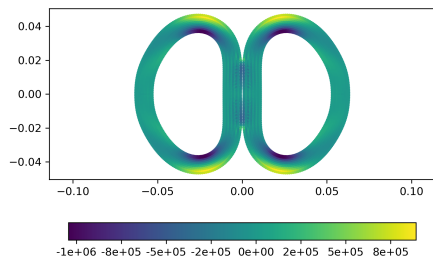
The projectile and the target are made of aluminium material. The projectile is 10mm in diameter and the rectangular target has a size of $2 \times 50\text{mm}$. The projectile and the target have the following material properties: density $\rho = 2785\text{kgm}^{-3}$, sound speed $c_0 = 5328 \text{ms}^{-1}$, shear modulus $G = 2.76 \times 10^7\text{kPa}$, yield modulus $Y_0 = 3.0 \times 10^5\text{kPa}$. The impact velocity is set to $V_0 = 3100.0\text{ms}^{-1}$. The initial particle spacing is $\Delta x = 0.5\text{mm}$. Here the aluminium follows an elastic-perfectly plastic constitutive model. In elastic perfectly plastic model, the material is assumed to be elastic up to the yield point and once the material reaches the yield point, there will be no



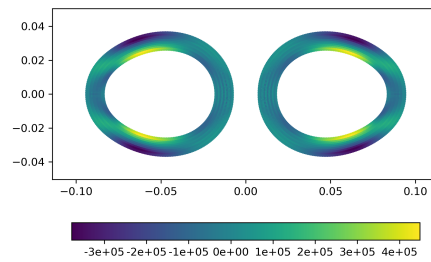
(a) $t = 2.5e-03$ sec



(b) $t = 4e-03$ sec

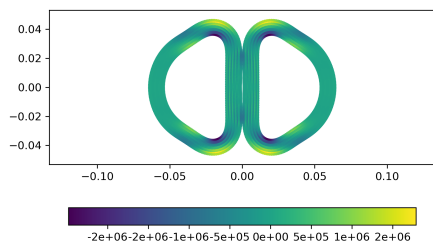


(c) $t = 7.3e-03$ sec

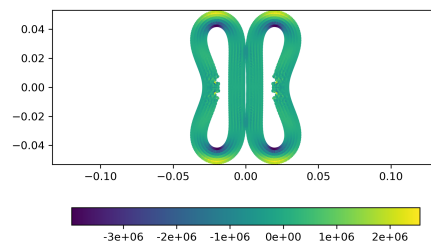


(d) $t = 1.45e-02$ sec

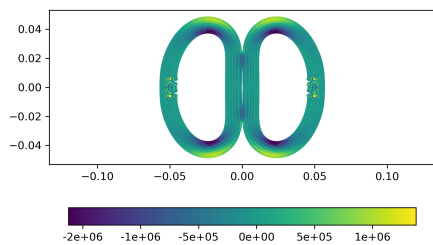
Figure 19: Rings with a Poisson ratio of 0.3975 colliding head on, simulated with CTVF using Sun 2019 PST.



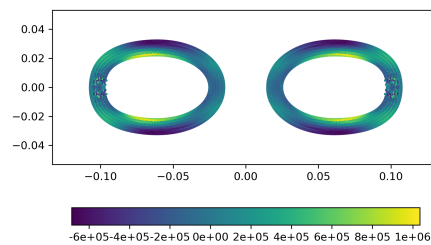
(a) $t = 2.5e-03$ sec



(b) $t = 4e-03$ sec

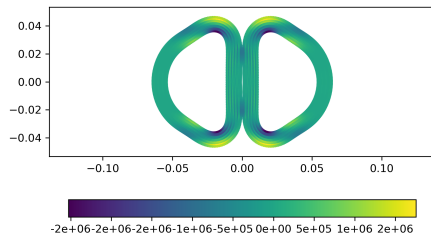


(c) $t = 7.3e-03$ sec

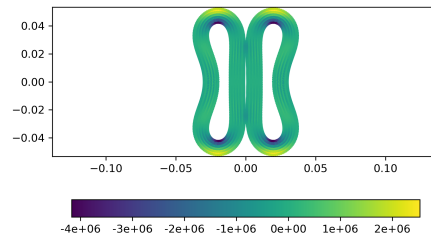


(d) $t = 1.45e-02$ sec

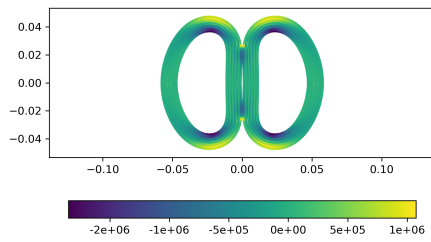
Figure 20: Rings with a Poisson ratio of 0.47 colliding head on, simulated with CTVF using Sun 2019 PST.



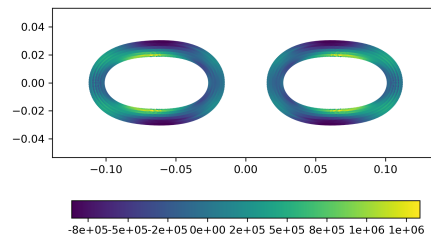
(a) $t = 2.5e-03$ sec



(b) $t = 4e-03$ sec



(c) $t = 7.3e-03$ sec



(d) $t = 1.45e-02$ sec

Figure 21: Rings with a Poisson ratio of 0.47 colliding head on, simulated with CTVF using IPST.

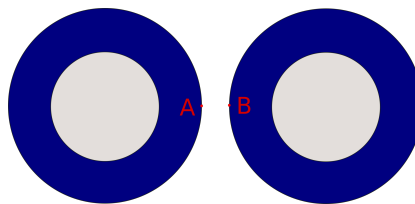


Figure 22: Schematic diagram of two rings colliding. Points A and B are marked.

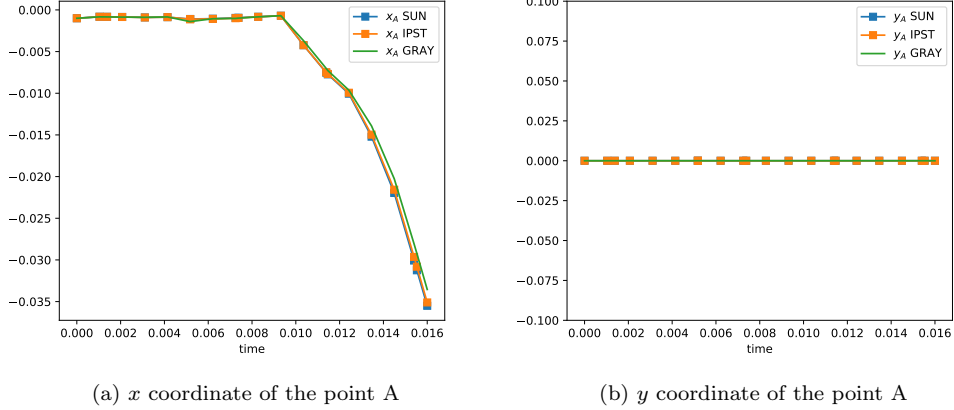


Figure 23: The evolution of the x and y coordinates of points A and B for the CTVF using the Sun 2019 PST, IPST, and compared with that of Gray [7].

further increase in the stress, and is bounded by a factor $\beta = \min\left(\frac{Y_0^2}{3J_2}, 1\right)$, where J_2 is calculated from $J_2 = \frac{1}{2}\boldsymbol{\sigma}' : \boldsymbol{\sigma}'$. We use an $\alpha = 1$ in eq. (28) in the current case.

Figure 24 shows the plots of cylinder impacting the structure at different time instants. This is computed using the particle shifting technique of Sun [20]. The color contour represents the pressure of the particles. The width of the hole created by the cylinder is 19.6mm. When computed using the GTVF scheme [18] the hole has a size of 19.8mm. In Howell and Ball [39], the value cited is 19.2mm. We can see, that the current scheme is closer to the one simulated by [39], which is taken as reference in [18].

5. Discussion and conclusions

The proposed CTVF scheme builds on the original TVF scheme of Adami et al. [17] and is as an improvement on the GTVF of Zhang et al. [18]. In addition it generalizes the implementation of the EDAC-SPH method [21] where the TVF formulation was used for internal flows and a separate WC-SPH formulation used for fluid flows with a free-surface. The current work proposes the addition of a few correction terms which improve the accuracy of the method as demonstrated in the earlier section. The addition of the terms imposes a small computational cost but compensates through the improved accuracy. As an example, in simulating the lid-driven cavity problem with a

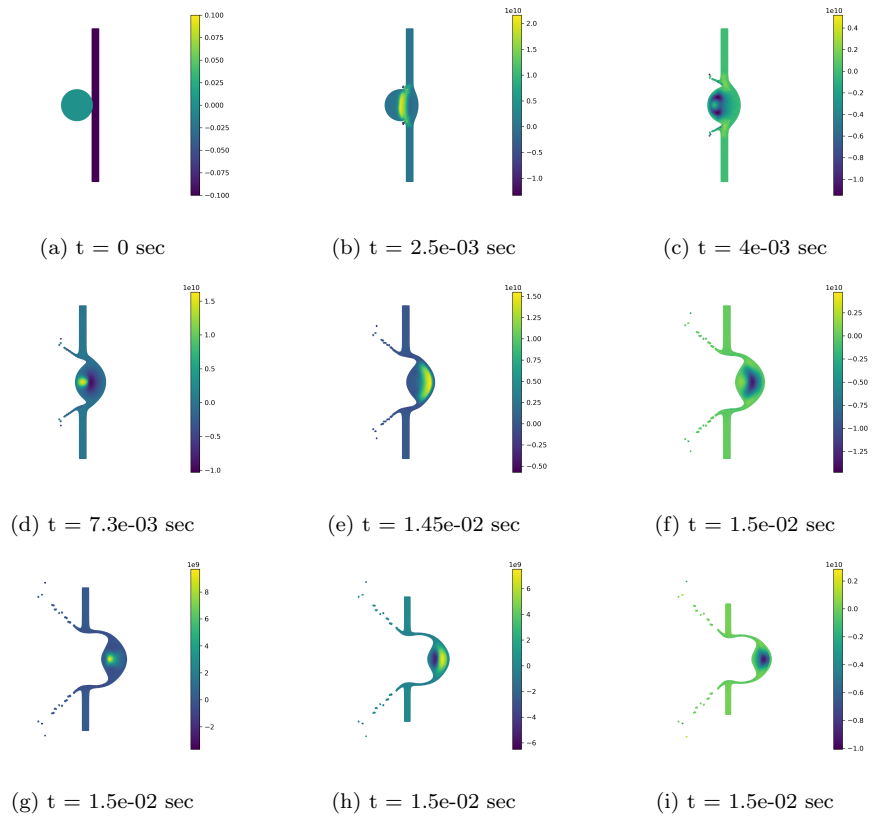


Figure 24: High velocity impact of cylinder on to a structure

resolution of 50×50 , the original EDAC scheme without any of the correction terms with a one step predictor corrector integrator takes 251 seconds for a time of 25 seconds, the new scheme with a kick-drift-kick scheme takes 293 seconds. Despite the change of the integrator this is a small increase in the performance. For solid mechanics problems we consider the colliding rings problem simulated for a total time of 0.016 seconds. This takes 98 seconds of time to simulate with the full CTVF scheme, and takes 73 seconds without the corrections (run on Intel i5-7400, quad core machine). Free-surfaces are handled carefully. The method produces smoother pressure fields due to the use of the EDAC scheme. Finally the method is robust to changes in the PST method used. This has been demonstrated using both the PST of Sun et al. [20] and the IPST of Huang et al. [15].

An important feature of the proposed scheme is that it works well in the context of both fluid mechanics and solid mechanics. For elastic dynamics we propose correction terms that improve the accuracy and robustness of the method. The GTVF [18] method fails when the PST method is changed as demonstrated in section 4.4, however the proposed method is more robust. Furthermore, our method uses the true velocity in order to compute the velocity gradient. The results of the uniaxial compression problem in section 4.5 suggest that that the proposed method is more accurate than the GTVF. The main difference between the GTVF and the current scheme in the context of solid mechanics is the addition of the correction terms to the continuity equation, the usage of momentum velocity \mathbf{u} in the computation of the velocity gradient, and the new particle shifting technique incorporation. We have found that the additional terms arising in the equation for the Jaumann stress rate eq. (4) has negligible influence and can be safely ignored. However, the computations in this work have included this term. The additional stress term in the momentum equation is negligible and has not been employed. We reiterate that for the fluid mechanics simulations the additional stress terms in the momentum equation are not negligible.

We note that for solid mechanics problems the method works well with either the traditional state equation used for the pressure evolution or the use of the EDAC equation. This does not make a significant difference for these problems since there is no additional damping added to the evolution equation for the deviatoric stresses. The EDAC evolution equation does make a significant improvement to the pressure evolution in the fluid mechanics problems as discussed earlier in [21].

The newly proposed method has not been applied to three dimensional

problems or to fluid structure interaction (FSI) problems. We believe that the method would be easier to use in the context of FSI since it can handle both fluids and solids in the same formulation. We propose to investigate these in the future.

Acknowledgment

The authors would like to thank Abhinav Muta for valuable discussions and feedback.

References

References

1. Lucy, L.B.. A numerical approach to testing the fission hypothesis. *The Astronomical Journal* 1977;82(12):1013–1024.
2. Gingold, R.A., Monaghan, J.J.. Smoothed particle hydrodynamics: Theory and application to non-spherical stars. *Monthly Notices of the Royal Astronomical Society* 1977;181:375–389.
3. Monaghan, J.J.. Smoothed Particle Hydrodynamics. *Reports on Progress in Physics* 2005;68:1703–1759.
4. Monaghan, J.J.. Simulating free surface flows with SPH. *Journal of Computational Physics* 1994;110:399–406.
5. Cummins, S.J., Rudman, M.. An SPH projection method. *Journal of Computational Physics* 1999;152:584–607.
6. Randles, P., Libersky, L.. Smoothed Particle Hydrodynamics: Some recent improvements and applications. *Computer Methods in Applied Mechanics and Engineering* 1996;139(1-4):375–408. doi:10.1016/S0045-7825(96)01090-0.
7. Gray, J., Monaghan, J., Swift, R.. SPH elastic dynamics. *Computer Methods in Applied Mechanics and Engineering* 2001;190(49-50):6641–6662. doi:10.1016/S0045-7825(01)00254-7; iSBN: 6139905443.

8. Rafiee, A., Thiagarajan, K.P.. An SPH projection method for simulating fluid-hypoelastic structure interaction. *Computer Methods in Applied Mechanics and Engineering* 2009;198(33):2785–2795. doi:10.1016/j.cma.2009.04.001.
9. Khayyer, A., Gotoh, H., Falahaty, H., Shimizu, Y.. An enhanced ISPH–SPH coupled method for simulation of incompressible fluid–elastic structure interactions. *Computer Physics Communications* 2018;232:139–164. doi:10.1016/j.cpc.2018.05.012.
10. Sun, P.N., Le Touzé, D., Oger, G., Zhang, A.M.. An accurate fsi-sph modeling of challenging fluid-structure interaction problems in two and three dimensions. *Ocean Engineering* 2021;221:108552. doi:10.1016/j.oceaneng.2020.108552.
11. Bui, H.H., Fukagawa, R., Sako, K., Ohno, S.. Lagrangian mesh-free particles method (sph) for large deformation and failure flows of geomaterial using elastic–plastic soil constitutive model. *International Journal for Numerical and Analytical Methods in Geomechanics* 2008;32(12):1537–1570. doi:<https://doi.org/10.1002/nag.688>.
12. Xu, R., Stansby, P., Laurence, D.. Accuracy and stability in incompressible sph (ISPH) based on the projection method and a new approach. *Journal of Computational Physics* 2009;228(18):6703–6725. doi:10.1016/j.jcp.2009.05.032.
13. Lind, S., Xu, R., Stansby, P., Rogers, B.. Incompressible smoothed particle hydrodynamics for free-surface flows: A generalised diffusion-based algorithm for stability and validations for impulsive flows and propagating waves. *Journal of Computational Physics* 2012;231(4):1499 – 1523. doi:10.1016/j.jcp.2011.10.027.
14. Skillen, A., Lind, S., Stansby, P.K., Rogers, B.D.. Incompressible smoothed particle hydrodynamics (sph) with reduced temporal noise and generalised fickian smoothing applied to body–water slam and efficient wave–body interaction. *Computer Methods in Applied Mechanics and Engineering* 2013;265:163 – 173. doi:10.1016/j.cma.2013.05.017.
15. Huang, C., Long, T., Li, S., Liu, M.. A kernel gradient-free SPH method with iterative particle shifting technology for modeling low-

- Reynolds flows around airfoils. *Engineering Analysis with Boundary Elements* 2019;106:571–587. doi:10.1016/j.enganabound.2019.06.010.
16. Ye, T., Pan, D., Huang, C., Liu, M.. Smoothed particle hydrodynamics (SPH) for complex fluid flows: Recent developments in methodology and applications. *Physics of Fluids* 2019;31(1):011301.
 17. Adami, S., Hu, X., Adams, N.. A transport-velocity formulation for smoothed particle hydrodynamics. *Journal of Computational Physics* 2013;241:292–307. doi:10.1016/j.jcp.2013.01.043.
 18. Zhang, C., Hu, X.Y.T., Adams, N.A.. A generalized transport-velocity formulation for smoothed particle hydrodynamics. *Journal of Computational Physics* 2017;337:216–232.
 19. Oger, G., Marrone, S., Le Touzé, D., de Leffe, M.. SPH accuracy improvement through the combination of a quasi-Lagrangian shifting transport velocity and consistent ALE formalisms. *Journal of Computational Physics* 2016;313:76–98. doi:10.1016/j.jcp.2016.02.039.
 20. Sun, P., Colagrossi, A., Marrone, S., Antuono, M., Zhang, A.M.. A consistent approach to particle shifting in the delta - Plus -SPH model. *Computer Methods in Applied Mechanics and Engineering* 2019;348:912–934. doi:10.1016/j.cma.2019.01.045.
 21. Ramachandran, P., Puri, K.. Entropically damped artificial compressibility for SPH. *Computers and Fluids* 2019;179(30):579–594. doi:10.1016/j.compfluid.2018.11.023.
 22. Clausen, J.R.. Entropically damped form of artificial compressibility for explicit simulation of incompressible flow. *Physical Review E* 2013;87(1):013309–1–013309–12. doi:10.1103/PhysRevE.87.013309.
 23. Antuono, M., Sun, P., Marrone, S., Colagrossi, A.. The δ -ale-sph model: An arbitrary lagrangian-eulerian framework for the δ -sph model with particle shifting technique. *Computers & Fluids* 2021;216:104806.
 24. Ramachandran, P.. PySPH: a reproducible and high-performance framework for smoothed particle hydrodynamics. In: Benthall, S., Rostrup, S., eds. *Proceedings of the 15th Python in Science Conference*. 2016:127 – 135.

25. Ramachandran, P., Bhosale, A., Puri, K., Negi, P., Muta, A., Adepu, D., Menon, D., Govind, R., Sanka, S., Sebastian, A.S., Sen, A., Kaushik, R., Kumar, A., Kurapati, V., Patil, M., Tavker, D., Pandey, P., Kaushik, C., Dutt, A., Agarwal, A.. PySPH: a Python-based framework for smoothed particle hydrodynamics. *arXiv preprint arXiv:190904504* 2020;URL: <https://arxiv.org/abs/1909.04504>.
26. Ramachandran, P.. automan: A python-based automation framework for numerical computing. *Computing in Science & Engineering* 2018;20(5):81–97. doi:10.1109/MCSE.2018.05329818.
27. Antuono, M., Colagrossi, A., Marrone, S., Molteni, D.. Free-surface flows solved by means of SPH schemes with numerical diffusive terms. *Computer Physics Communications* 2010;181(3):532 – 549. doi:<https://doi.org/10.1016/j.cpc.2009.11.002>.
28. Morris, J.P., Fox, P.J., Zhu, Y.. Modeling low reynolds number incompressible flows using sph. *Journal of computational physics* 1997;136(1):214–226.
29. Sun, P., Colagrossi, A., Marrone, S., Zhang, A.. The δ plus-sph model: Simple procedures for a further improvement of the sph scheme. *Computer Methods in Applied Mechanics and Engineering* 2017;315:25–49.
30. Xu, R., Stansby, P., Laurence, D.. Accuracy and stability in incompressible sph (isph) based on the projection method and a new approach. *Journal of computational Physics* 2009;228(18):6703–6725.
31. Marrone, S., Colagrossi, A., Le Touzé, D., Graziani, G.. Fast free-surface detection and level-set function definition in SPH solvers. *Journal of Computational Physics* 2010;229(10):3652–3663. doi:10.1016/j.jcp.2010.01.019.
32. Muta, A., Ramachandran, P., Negi, P.. An efficient, open source, iterative ISPH scheme. *Computer Physics Communications* 2020;255:107283. doi:10.1016/j.cpc.2020.107283.
33. Adami, S., Hu, X., Adams, N.. A generalized wall boundary condition for smoothed particle hydrodynamics. *Journal of Computational Physics* 2012;231(21):7057–7075. doi:10.1016/j.jcp.2012.05.005.

34. Ghia, U., Ghia, K.N., Shin, C.T.. High-Re solutions for incompressible flow using the Navier-Stokes equations and a multigrid method. *Journal of Computational Physics* 1982;48:387–411.
35. Koshizuka, S., Oka, Y.. Moving-particle semi-implicit method for fragmentation of incompressible fluid. *Nuclear science and engineering* 1996;123(3):421–434.
36. Landau, L.D., Lifshitz, E.M., Sykes, J.B., Reid, W.H., Dill, E.H.. Theory of elasticity: Vol. 7 of course of theoretical physics. *Physics Today* 1960;13(7):44–46. doi:10.1063/1.3057037.
37. Das, R., Cleary, P.W.. Evaluation of accuracy and stability of the classical sph method under uniaxial compression. *Journal of Scientific Computing* 2015;64(3):858–897.
38. Swegle, J.W., Hicks, D.L., Attaway, S.W.. Smoothed particle hydrodynamics stability analysis. *Journal of computational physics* 1995;116(1):123–134.
39. Howell, B., Ball, G.. A free-lagrange augmented Godunov method for the simulation of elastic–plastic solids. *Journal of Computational Physics* 2002;175(1):128–167.